

Coaxial Ceramic Direct Ink Writing on Heterogenous and Rough Surfaces: Investigation of Core-Shell Interactions

*Domenic Cipollone, Javier. A Mena, Katarzyna Sabolsky, Edward M. Sabolsky, Konstantinos A. Sierros**

Department of Mechanical and Aerospace Engineering, West Virginia University, Morgantown, WV 26506-6106, USA

KEYWORDS: Coaxial; 3D Printing; Sensor; Ink Design; Flow Stability

ABSTRACT

In this work, coaxial direct ink writing enables the printing of sensitive or encapsulated materials onto heterogenous and rough substrates. While encasing the core fluid within a stiff ceramic shell, continuity may be maintained, even while printing onto conventionally challenging substrates. Here, we report the development of a coaxial ceramic direct ink writing suite and explore co-flow interrelationships based on microfluidic principles. A coaxial nozzle is designed

to facilitate the co-extrusion of an alumina shell, while indium-tin-oxide inks constitute the core. In this manner, a core-shell ceramic element may be printed onto rough substrates for future high temperature applications. Colloidal inks are engineered to provide the required rheological and sintering performance. Moreover, flow simulations in conjunction with microfluidic co-flow principles are used to explore the coaxial printing processing space, thus controlling the core-shell architectures. Physical modeling is further used to analyze core deformations and eccentricity. Simulations are validated experimentally, and the analyses used to deposit coaxial ceramic features onto heterogenous, high temperature ceramic substrates.

1. Introduction

Industry 4.0 refers to a new phase in the industrial revolution which focuses heavily on interconnectivity, automation, machine learning, and real-time data acquisition.¹ Within this phase, real-time structural health monitoring is critically important, across both low and high temperature environments. However, in high temperature environments (>600 °C), integration of sensing elements *in-situ* remains a challenge.^{2,3} For example, in furnace refractory, the sensing element's substrate surface may be highly heterogenous and irregular, featuring multimodal aggregate distributions. The resulting protrusions pose a significant challenge to forming intimate sensor-substrate interfaces. Additionally, the substrate protrusions force any *in-situ* deposition technique to adapt to the surface, introducing further manufacturing and operational challenges. Ideally, the sensing material and its respective substrate must both conform to the deposition substrate, intimately bond, and shrink minimally to prevent stress induced failures. Moreover, an embedded sensing element acts as a foreign body, and typically opens the door for manufacturing defects, premature mechanical failures, or sensor delamination.^{4,5} Additive manufacturing,

specifically coaxial direct ink writing, offers a potential unique solution. Through an additive approach, these manufacturing challenges may be addressed from a materials perspective, instead of an operational perspective.

Direct ink writing (DIW), an extrusion based additive manufacturing technique, enables the *in-situ* deposition of sensing materials using pneumatic pressure. To date, DIW has been utilized to produce a range of devices, such as wearable electronics⁶, biomedical devices⁷⁻⁹, and ceramics¹⁰⁻¹². Owing to the lax material constraints, simplified manufacturing technique, and the absence of heat or environmental controls, DIW enables both in-line integration into manufacturing and the deposition onto a diverse array of substrates. In these instances, ink-substrate compatibility is addressed through materials selection and ink design. Overall, among extrusion-based techniques, DIW is believed to be the most versatile in terms of materials development and implementation, enabling the fabrication of complex 2.5D and 3D structures by formulating and extruding inks with tailored rheology and surface properties. However, printing onto rough and heterogeneous substrates *in-situ* with irregularities of a few millimeters remains challenging. Without proper protection or shielding, functional sensor components may suffer discontinuities.

Coaxial DIW, in which two or more materials are simultaneously extruded through the same orifice, provides a method of sensitive material encapsulation. To date, numerous researchers have employed the technique to fabricate core-shell biomaterials¹³⁻¹⁵, wearable devices¹⁶, and flexible electronics¹⁷. In many cases, the coaxial method provides enhanced interfacial stability and adhesion, as well as offers a protective casing for the active electronic or biomaterial. However, very few applications involve ceramic materials. Moreover, the limited reports of coaxial ceramic materials frequently involve micro solid oxide fuel cells. In these instances, the fuel cells are fabricated through conventional extrusion techniques and do not integrate substrate challenges.¹⁸⁻

²⁰ Additionally, to date, a vast majority of coaxial DIW applications involve both soft and miscible materials intended for use in ambient conditions.^{16,21} The use of these materials simplifies the ink design process and removes any concerns of shrinkage, post-processing challenges, or core-shell coefficient of thermal expansion mismatch.

Here, we report the ink engineering, flow characterization, and deposition of functional ceramics through coaxial DIW. The coaxial process is utilized to shield and deposit a conductive core ceramic onto a heterogenous high temperature ceramic substrate. A pH adjusted alumina shell ink is used to encapsulate conductive indium tin oxide (ITO) cores. Moreover, the use of a bimodal alumina particle distribution reduces shrinkage and enables compatibility with dense substrates. The inks are engineered such that the hydrophobic core ink maintains a high-fidelity interface with respect to the hydrophilic shell. Through this coaxial approach, the ink may be extruded onto both planar and rough substrates, while maintaining core continuity through the viscoelastic shell. A stereolithography (SLA) printed coaxial nozzle assembly, connected via Leur lock to the functional ceramic inks, enables the precise deposition of a range of core diameters and accommodates a range of core ink viscosities. Considering similarities to microfluidic co-flow, ink processing is assessed through several dimensionless numbers and flow rate ratios to ascertain the governing material and process parameters. Moreover, core deformations are analyzed through a force balance, providing a route to re-engineer optimized inks. The co-flow and interface are characterized through COMSOL flow simulations and used to guide experimentation. SEM and EDX analysis are then used to characterize the sintered interface. Finally, characterization of the coaxial element's resistance during temperature cycling is used to demonstrate the potential and functionality of the material suite.

2. Materials and Experimental Methods

2.1 Materials

Fine alumina (A 16 SG) and coarse alumina (A 20 SG) particles were purchased from Almatris (Leetsdale, PA USA) and used as received to serve as the ink's particulate phase. Methylcellulose (Methoxyl content 28-32%) was purchased from Sigma Aldrich (St. Louis, MO USA) and deionized water was used as a solvent. Polyacrylic acid powder (avg. MW 1800) was purchased from Sigma Alrich (St. Louis, MO USA) and used as a surfactant and pH modifier. To further adjust the ink pH and tailor the particle surface charge and ink stiffness, sodium hydroxide (1 N, Sigma Aldrich, St. Louis, MO USA) was used for titration. Finally, indium tin oxide particles (325 mesh, In₂O₃ 90%, SnO₂ 10%) were purchased from Sigma Aldrich (St. Louis, MO USA) and used as received. A Johnson Matthey (London, UK) ink vehicle was used as the core ink binder solution and used without modification.

2.2 Ink Synthesis

Alumina core ink preparation began with the synthesis of a 1.5 wt% aqueous methylcellulose binder solution. A 40 wt% aqueous polyacrylic acid solution was then mixed and added to the binder solution. Coarse and fine alumina were added in a 3:1 volume ratio to bring the alumina volume fraction to approximately 52%. Upon addition of half of the alumina, the ink was mixed in a planetary mixer (Thinky AR200, Thinky USA) for 2 minutes, followed by wand sonication (Model 50 Sonic Dismembrator, Fischer Scientific) for 20 seconds. The remainder of the alumina was then added, and the planetary mixer and sonication procedure repeated. Finally, the ink pH was measured using a digital benchtop pH meter (Orion Star A211, Thermo Scientific). The pH was adjusted as necessary using a 1 N NaOH hydroxide solution (Sigma Aldrich, St. Louis, MO USA). The final ink consisted of approximately 52 vol% alumina, 4 vol% PAA stabilizer solution, and 34 vol% methylcellulose solution.

Two conductive core ITO inks were prepared by mixing the required ITO volume into a Johnson Matthey Ink vehicle. ITO inks were prepared such that the solids volume fraction represented 15 vol% and 20 vol%, respectively. In each case, the powder was added to the ink vehicle, mixed within the planetary mixer and wand sonicated for 20 seconds. All inks (core and shell) were then briefly degassed in the planetary mixer and loaded into printing syringes (Nordson EFD, Providence, RI USA) for printing.

2.3 Coaxial Printing

The coaxial nozzles were printed using a Formlabs (Somerville, MA) Form 3 stereolithography printer with a 50 μm layer height. The outer diameter of the nozzle was 1.5 mm with a 14-degree taper. A tapered design was chosen to reduce the required printing pressure and prevent clogging within the nozzle. Flow analysis of the tapered nozzle may be found in the supporting information (Figure S1). The inner nozzle assembly, consisting of a Nordson 3 cc printing syringe with a 410 μm or 510 μm nozzle, was then press fit into the printed coaxial assembly. Finally, a 30 cc Nordson syringe was filled with the alumina shell ink and attached via Leur lock to the printed nozzle assembly.

A Nordson Ultimius V pressure dispenser was used to dispense both the shell and core inks. Printing was performed using a Nordson JR23000N robotic arm. The applied pneumatic pressure for both the core and shell inks varied from 0.05-0.6 MPa to facilitate studies over a range of flow rate and viscosity ratios. For flow and fidelity characterization, samples were printed onto Mylar. After identifying processing regions, samples were then printed directly onto heterogenous ceramic substrates.

2.4 Characterization

Rheology, both steady-state and oscillatory, was characterized using an RMS-800 Rheometer (Rheometric Scientific, Piscataway, NJ USA) with a 1 mm gap and 25 mm parallel plate. Sandpaper was attached to both plates to prevent slip. Strain sweeps, used to characterize the shear moduli and stiffness, were performed at 10 rad/s from 0.02 – 50% strain. Steady state measurements, used to characterize the viscosity and dynamic yield stress, were performed from 0.01 – 50 1/s. The dynamic yield stress critically provides insight into how much stress the filament or feature can endure after printing without causing deformation.

Core and shell dimensional measurements were obtained using a digital microscope (Dino-Lite Edge, Los Angeles, CA USA). Cross-sectional areas were characterized through built-in Dino-Lite automatic edge tracing tools. Cross-sectional scanning electron microscopy (SEM) and energy dispersive X-ray spectroscopy (EDX) was performed using a Hitachi S-4700 electron microscope after briefly sputtering the samples with platinum. Finally, when feasible, surface tension was measured with the pendant drop method using the ImageJ (National Institute of Health) Drop Analysis Plugin.

2. Results and Discussion

3.1 Ink Engineering

Critical to the success of DIW, specifically in coaxial applications, is the synthesis of a stiff ink which provides shape retention and high fidelity. In most cases, the objective is to obtain a critical threshold of the storage modulus (G') which reduces slumping and maintains printed fidelity. Values of $G' > 200$ Pa tend to provide adequate stiffness and self-supporting properties.²²⁻²⁴ The stiffness of an ink may be tailored through several levers, including increasing the particulate phase volume fraction^{25,26}, employing a high viscosity binder solution²⁷, or through tailoring colloidal interactions^{28,29}. Several groups have engineered extrudable ceramic inks with limited drying and

sintering shrinkage through exploration of the particulate phase volume fraction. These works suggest volume loadings of greater than 50% to be suitable to prevent cracking during drying and promote shape retention.³⁰ Moreover, pH adjustment may be used to further tune particle interactions. Consequently, the ink stiffness may be tailored by an order of magnitude or more, helping to achieve the threshold storage modulus.^{31,32} As a final constraint of DIW, the ink must be sufficiently shear-thinning, and feature both limited drying shrinkage and sintering shrinkage for compatibility with dense substrates. Overall, an appropriately synthesized ink should have: 1) limited drying and sintering shrinkage to prevent cracking, 2) levers to tune the stiffness (G'), and 3) high fidelity and shape retention.

First, to address sintering and drying shrinkage, a bimodal alumina shell ink was synthesized. When fine particles are added to coarse the maximum packing fraction (Φ_m) increases. This effect on Φ_m has been shown to be especially pronounced on particles with a size ratio of $\sim 7:1$, i.e. the coarse particles are approximately 7 times the size of the fine.³³ Therefore, coarse and fine particles (~ 3 and ~ 0.5 μm) which fit a 6:1 size ratio were chosen.

To engineer the stiffness through colloidal interaction, the alumina shell ink was prepared with the addition of polyacrylic acid (PAA), which provides steric repulsion. The main functional group of PAA chains are carboxyl ($-\text{COOH}$) groups. As the pH of a PAA solution increases, functional groups tend to dissociate. During synthesis, the alumina ink pH was maintained at approximately 5.5. The pK_a of polyacrylic acid is approximately 4.5, above which carboxylic groups will dissociate, and form ($-\text{COO}^-$) groups.^{34,35} As pH increases to 6, PAA is nearly completely ionized with a degree of dissociation equal to 0.97.³⁴ However, the zeta potential and surface charge of alumina in acidic conditions is positive.³⁵⁻³⁸ Therefore, the polyacrylic acid may adsorb to the alumina particle surface electrostatically or through hydrogen bonding of ($-\text{COOH}$) if pH is

monitored to maintain alumina surface hydroxyl (-OH) groups. The steric repulsion provided by the adsorbed polymer is sufficient to prevent agglomeration of the microparticles, enabling consistent printing and processing. Further particle dispersion is induced through hand sonication following the planetary mixing stages.

However again, some degree of flocculation and controllable stiffness is needed for DIW, particularly in ink systems with relatively low organic binder content. Inducing flocculation, and increasing particle interaction, increases the particle-particle resistance to flow (viscosity), which is typically provided through viscous polymers. Through titration with NaOH following ink mixing, the alumina ink stiffness could be tailored by approximately one order of magnitude (Figure 1a). The point of zero charge (i.e. at which the zeta potential is zero and particles particle surface charge is balanced) is well documented and is approximately 8 - 9 pH.^{37,39} As the point of zero charge is approached, particles will tend to flocculate, inducing an increase in viscosity and stiffness. Figure 1a reveals that as the pH increases from 7.5 to 7.9, ink stiffness increases. However, upon passing the point of zero charge, ink stiffness again decreases as particles regain electrostatic repulsion. Therefore, inks were synthesized with a final adjusted pH of approximately 7.9 for printing.

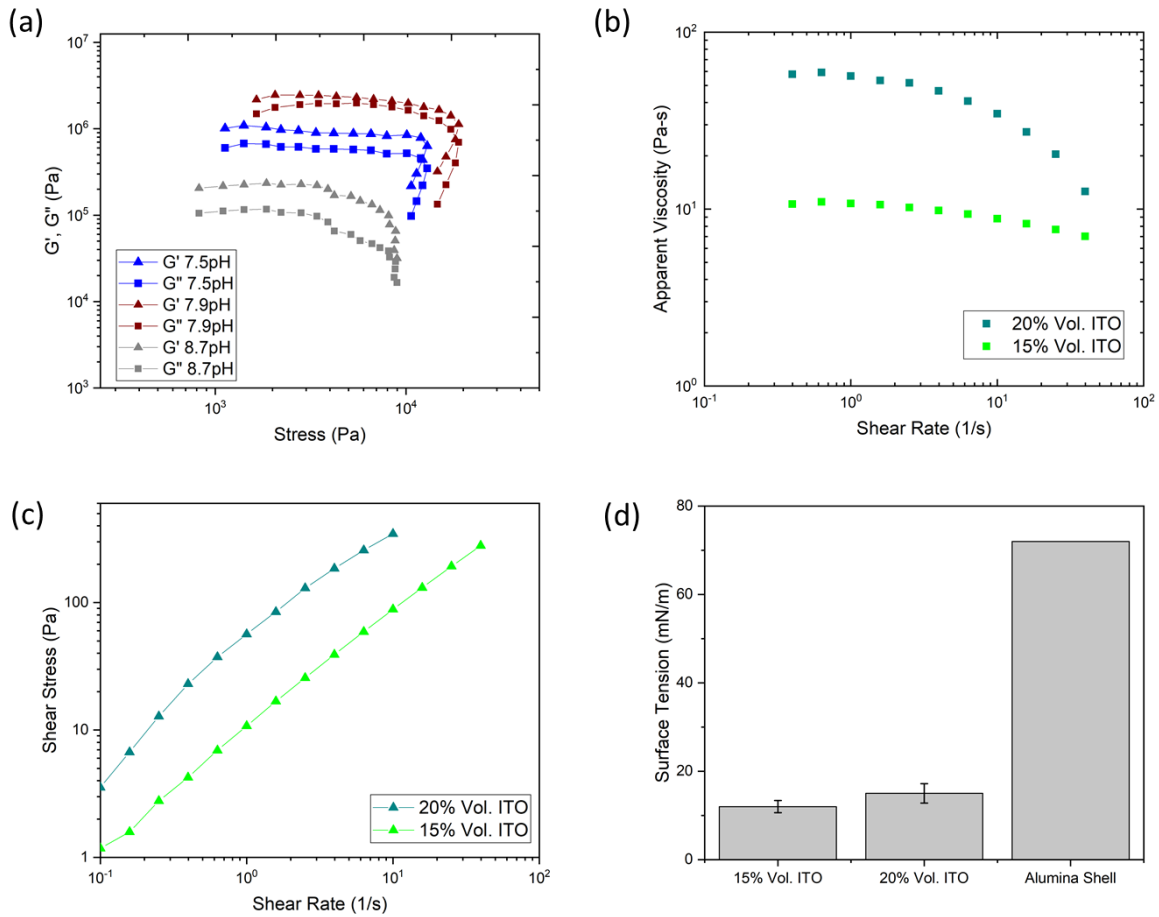


Figure 1. Core-shell ink rheological data and surface characterizations. (a) Storage and loss moduli vs. shear stress of the alumina shell inks, (b) apparent viscosity vs. shear rate, (c) shear stress vs. shear rate of the ITO core inks and (d) pendant drop measured surface tension.

Inks were further characterized with steady-state rheology and application of the Herschel-Bulkley model (eq 1):

$$\tau = \tau_y + K\dot{\gamma}^n \quad (1)$$

where τ is the shear stress, τ_y is the yield stress, K is the consistency index ($Pa \cdot s^n$), and n is the shear-thinning index.⁴⁰ When $n < 1$, the ink exhibits shear-thinning behavior, while when $n = 1$ the ink exhibits Newtonian behavior. All core inks and the 7.9 pH alumina ink show varying

degrees of shear thinning behavior which tends to increase as the particle loading increases (Figure 1b and Figure 1c). Moreover, the yield stress is shown to increase with an increase in the particle volume fraction (Table 1). Notably, the 15 vol% ITO ink, considering both the flow curve and the shear thinning index, tends towards Newtonian behavior.

Table 1. Herschel-Bulkley parameters for the selected alumina shell ink and the ITO core inks.

Ink	Yield Stress (Pa)	K ($Pa \cdot s^n$)	n
Alumina Shell	755	832	0.41
20% vol. ITO	7.16	62.60	0.76
15% vol. ITO	1.25	13.43	0.83

Finally, a challenging aspect of yield-stress fluid characterization involves the calculation of the surface tension. For the ITO inks, the pendant drop method remained feasible. However, for significantly stiffer fluids, a droplet is challenging to form. It has been shown that the surface tension of a yield stress fluid may be reasonably approximated by that of the solvent medium.⁴¹ In the case of the aqueous alumina ink, the surface tension was taken as that of water (72 mN/m) (Figure 1d).

3.2 Co-flow Stability and Characterization

In microfluidic co-flow systems, stable co-flow is achieved through the balancing of fluid instabilities and competing viscous and inertial forces. At the micron length scale, and on the scale of the system of this study, interfacial and viscous effects dominate bulk and inertial forces.⁴² Typically in coaxial co-flow systems, one of two events occurs: the formation of droplets or the formation of a continuous jet. The Plateau Rayleigh instability is responsible for many modes which result in dripping, as surface tension forces seek to minimize the interfacial area.⁴²⁻⁴⁴ In

addition to the forces of interfacial tension, the viscous and inertial forces suppress modes of deformation which result in droplet generation, instead promoting elongated jets. A general force balance of microfluidic co-flow is shown in **¡Error! No se encuentra el origen de la referencia..**

$$F_{gravitational} + F_{inertial} + F_{viscous} = F_{interfacial} \quad (2)$$

During unstable co-flow, three stages proceed: the meeting of the fluids to form an immiscible interface, deformation of the interface to an unstable state, and ultimately deformation of the interface into droplets or widening jets. Dimensionless numbers, such as the Capillary number (Ca) and Weber number (We) (eqs 3 and 4) integrate the interfacial forces and are thus pertinent to the characterization of stable co-flow regimes:

$$Ca = \frac{\eta u}{\gamma} \quad (3)$$

$$We = \frac{\rho u^2 L}{\gamma} \quad (4)$$

where η is the viscosity, ρ is the fluid density, u is the flow velocity, and γ is the surface tension.⁴⁴ Moreover, to assess the influence of inertial and viscous forces on stable co-flow, the generalized Reynold's number, applicable to non-Newtonian fluids (Re) may be used:

$$Re_G = \frac{\rho u^{2-n} L^n}{K \left(\frac{3n+1}{4n} \right)^n \cdot 8^{n-1}} \quad (5)$$

where K is the Herschel-Bulkley consistency index, n is the shear-thinning index, and u is the flow velocity. Finally, the viscosity ratio λ and flow rate ratio φ of the outer (shell) and inner (core) phases are two additional dimensionless quantities useful in describing co-flow:

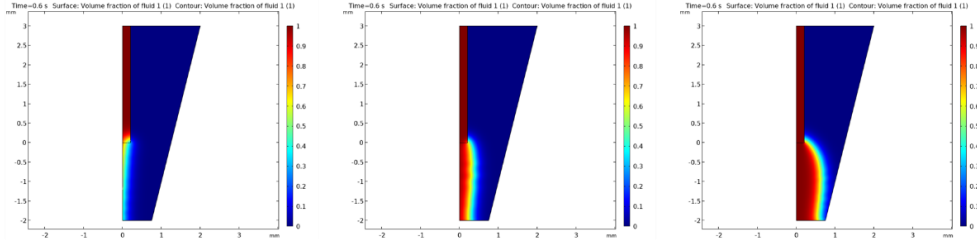
$$\lambda = \frac{\eta_o}{\eta_i} \quad (6)$$

$$\varphi = \frac{Q_o}{Q_i} \quad (7)$$

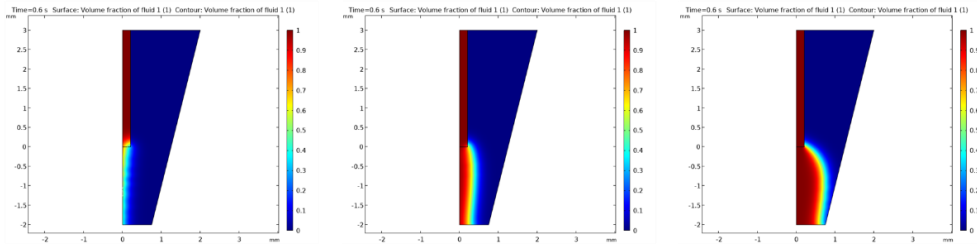
To develop initial understanding of the coaxial extrusion process and study the effects of the flow rate and viscosity ratio, COMSOL Multiphase flow was used. Within the flow simulation package, the Level Set method provides a simplified approach to modeling the co-flow of two immiscible fluids. In this case, the immiscible core-shell interface could be tracked from the initial flow merge to the nozzle exit. **¡Error! No se encuentra el origen de la referencia.S2** (supplementary information) shows the modeling geometry used. The analysis, using axial symmetry, tracks the initial interfacial interaction and fluid flow within the coaxial nozzle. Fluid properties obtained from the rheological and surface tension characterizations were used to model the non-Newtonian flow (Table 1). Further detail regarding application of the Level Set method and material inputs may be found in the supporting information.

From simulation, and later confirmed experimentally, the core diameter is a logarithmic function of the flow rate ratio, i.e. the diameter logarithmically decreases as the flow rate ratio (φ) increases (Figure 2). The flow is seen to remain stable for a wide range of simulated flow rate ratios [0.25 – 25]. Additionally, the 20 vol% ITO core ink maintains a larger exit diameter, attributable to the greater dynamic yield stress versus the 15 vol% ITO formulation. Notably, as the flow rate ratio decreases, the core flow does exhibit a slight widening towards the nozzle exit relative to the mid-stream diameter (Figure 2).

20% vol. ITO



15% vol. ITO



$$\frac{Q_o}{Q_i} = 25$$

$$\frac{Q_o}{Q_i} = 2.5$$

$$\frac{Q_o}{Q_i} = 0.25$$

Decreasing Flow Rate Ratio

Figure 2. Flow simulations of the 20 vol% ITO (top) and 15 vol% ITO (bottom) across a range of flow rate ratios. No instability is observed within the nozzles. However, a logarithmic increase in core exit diameter is observed with a decreasing flow rate ratio. The 20 vol% core ink maintains a larger exit diameter.

Following the preliminary simulations, samples with flow rate ratios ϕ ranging from 2-180 were printed to validate the simulations. Specifically, the effects of various flow conditions on the core diameter and stability were examined. In most instances, the flow rate ratio was varied simply by varying the core diameter flow rate for both core ink formulations. Due to some intermittent inconsistencies in the shell ink and resultant challenges in calculating the pressure drop, the alumina flow rate was calculated following printing. In these cases, the cross-sectional area and print length were used to calculate the volume deposited. From the volume and print time, the

empirical volumetric flow rate was calculated. For the core ink, the flow rates were calculated numerically using eq 8:

$$Q = \frac{\pi D_c^3}{8K^{\frac{1}{n}}} \tau_w^{\frac{1}{n}} \quad (8)$$

where Q is the flow rate, D_c is the core nozzle diameter, K is the Herschel Bulkley consistency factor, n is the shear-thinning index, and τ_w is the maximum shear stress at the nozzle wall, calculated using eq 9:

$$\tau_w(r) = \frac{\Delta P}{2L_c} r \quad (9)$$

where ΔP is the applied pressure, L_c is the length of the core nozzle, and r is the nozzle radius. Shear stress will be maximized at the wall ($r = R$) and minimized at the center ($r = 0$).⁴⁵ Using the maximum calculated flow rate Q , the shear rate $\dot{\gamma}$ was then calculated using eq 10:

$$\dot{\gamma} = \frac{3n + 1}{4n} \frac{4Q}{\pi R^3} \quad (10)$$

For shear-thinning fluids such as the alumina and ITO inks, the viscosity varies with the applied shear rate or shear stress. Using the Herschel-Bulkley parameters obtained through rheological characterization and the calculated shear rate obtained through Eq. 10, the apparent viscosity was calculated using eq 11:

$$\eta = \frac{\tau_0}{\dot{\gamma}} + K \cdot \dot{\gamma}^{(n-1)} \quad (11)$$

where K is again the consistency factor, τ_0 is yield stress, and n is the shear thinning index. Using the numerically or empirically derived flow rates, flow velocities, and calculated apparent viscosities, the Capillary, Weber, and Reynold's numbers were explored to devise stable co-flow processing regions (**¡Error! No se encuentra el origen de la referencia.3**).

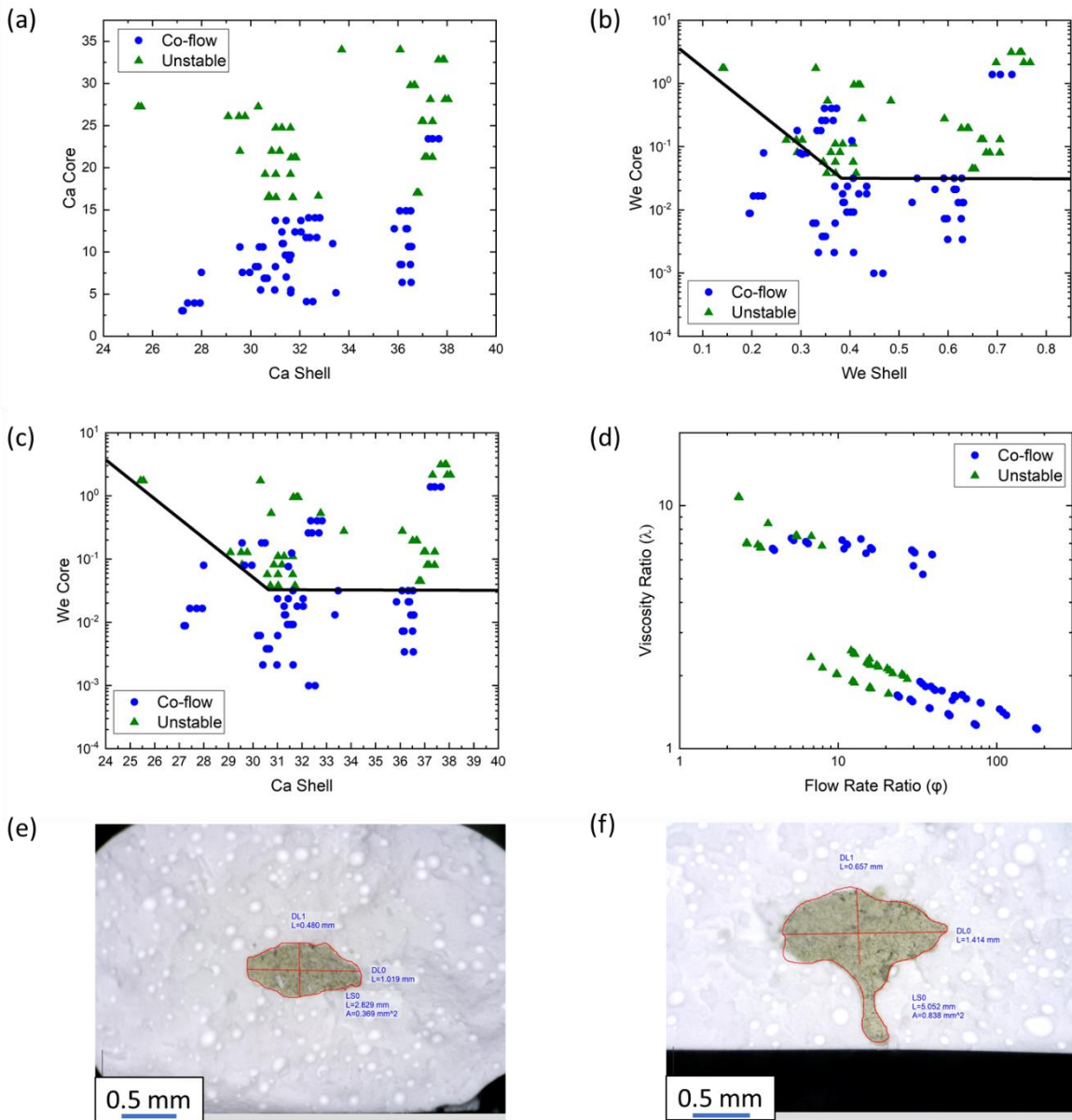


Figure 3. (a) Comparison of the core and shell capillary numbers, (b) core and shell Weber numbers, (c) core Weber number and shell Capillary number, (d) flow stability characterized through viscosity and flow rate ratios, (e) a 'stable' coaxial print, and (f) an unstable coaxial core cross-section.

Notably, in terms of processing, direct comparison of the core and shell generalized Reynold's numbers did not provide insight into flow stability, with no obvious demarcation between stable

and unstable co-flow (Figure S5). In all cases, the $Re \ll 1$, which confirms highly laminar flow. However, in agreement with the flow simulations, for a relatively fixed viscosity ratio, stable co-flow is maintained at high flow rate ratios ($\varphi \gg 1$).

The Capillary number of the shell ink represents the magnitude of the viscous shear forces relative to the interfacial tension, while the Weber number represents the magnitude of the inertial forces relative to surface tension. Within the coaxial system, the core ink experiences viscous shear and inertial forces from the shell, as well as the internal inertial and viscous forces. Figure 3a reveals steady co-flow across a moderate range of shell Ca numbers. However, upon reaching a core Ca of ~ 15 , co-flow stability is lost within the core. As a result, the combination of both core and shell inertial forces produces flow instabilities and perturbations (Figure 3f). Likewise, Figure 3b reveals co-flow stability across moderate core Weber numbers, with minimal variation in the shell inertial forces acting on the core. However, when $We_{core} + We_{shell} \geq O(10^{-1})$, flow instability results. These results are in general agreement with previous reports of co-flow stabilities, in which dripping to jetting transitions are mapped through relationships of the We_{core} and Ca_{shell} .^{43,46}

Due to the opacity of the system, the true form of flow instability is currently unknown. Likely, however, the perturbations observed may be the result of a widening jet in which the inertial and viscous forces dominate those from interfacial tension.⁴³ This hypothesis is supported by optical cross-sectional measurements which reveal not droplets, but continuous printed core filaments. Moreover, the flow simulations do reveal a more pronounced core widening at the coaxial nozzle exit as flow rate ratios decrease (Figure 4a). From experiments, the unstable co-flow groupings tend to appear as the velocity ratio (u_o/u_i) approaches one (Figure 4b). In this instance, the core fluid experiences a relative deceleration. When coupled with the critical Capillary number of ~ 15 ,

a stable to unstable flow transition is observed. Moreover, widening jets are reported in instances in which the inner fluid $Ca > 1$ if the $Re < 1$.⁴⁷ These conditions hold true across all samples. Though simulation and experimentation strongly support the widening jet hypothesis, further investigation of transparent non-Newtonian materials will be needed to validate the instability. Additionally, future areas of study may look to harness these instabilities, both dripping and widening jet, to tailor core architectures or promote droplet encapsulation. For example, viscous shear thinning hydrogels may be used to encapsulate drugs, while droplet generation may be used to enable high fidelity graded structural elements.

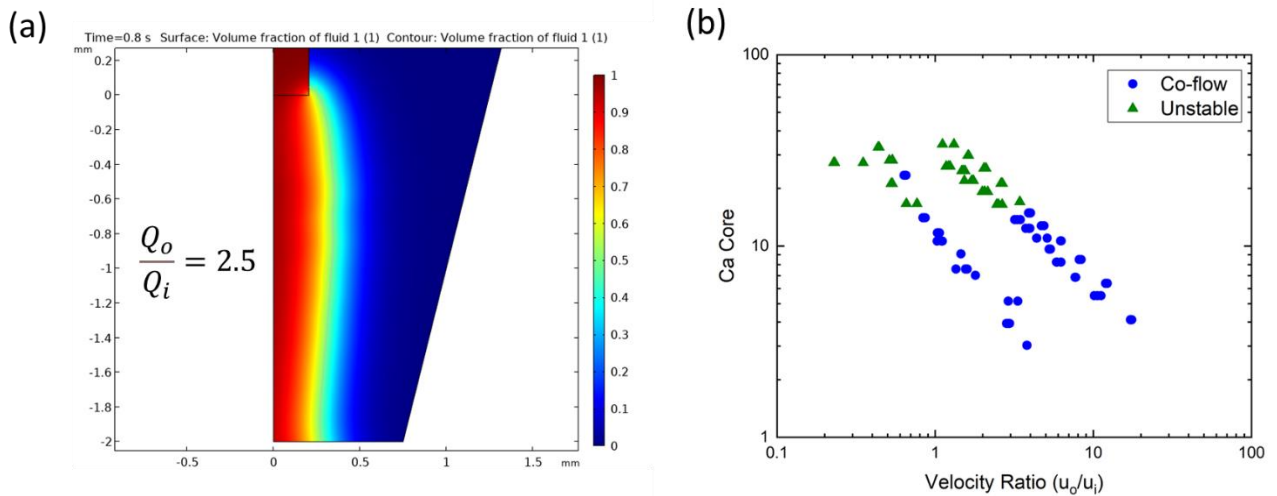


Figure 4. (a) Magnified flow simulation of the 15 vol% ITO at $\varphi = 2.5$ revealing a widening core jet towards the nozzle exit. (b) State map of the core Capillary number versus the velocity ratio. As the velocity ratio decreases and the viscous forces reach a critical threshold, flow instability, likely in the form of a widening jet, results.

3.3 Core Fidelity and Deformation

The flow simulations suggest a logarithmic decrease in core diameter as a function of increasing flow rate ratio. Due to the eccentricity of the core observed experimentally, which was not captured

within flow simulations, an effective diameter was used in empirical diameter versus φ calculations. This value captures the total cross-sectional area and derives an equivalent circle and associated diameter. This measurement results in a clear logarithmic trend, in which the 20 vol% ITO core ink maintains a larger effective diameter than the lower viscosity 15 vol% ITO ink across all flow rate ratios, as observed in simulations (Figure 5a). This is likely attributable to the larger dynamic yield stress of the 20 vol% ITO, providing a greater resistance to external deformation.

Aside from the inertial, viscous, and capillary forces acting on the core during extrusion, gravitational forces may induce core deformation and eccentricity following printing. To explore this potential relationship and derive a physical representation of core deformation, a balance of inward and outward radially opposed forces was analyzed. Within the core, the dynamic yield stress acts to resist deformation, counteracted by the gravitational pressure and capillary forces of the shell (Figure 5b). Therefore, a dimensionless quantity, \mathcal{E} , was adapted from M'Bharki et al., which was previously used to quantify the printability of boehmite gels.⁴¹ In the case of coaxial printing, the adapted quantity \mathcal{E} represents the ratio of the core dynamic yield stress (τ_y^{dyn}) to the sum of the shell gravitational and capillary forces (eq 12):

$$\mathcal{E} = \frac{\tau_y^{dyn}}{(\rho gh + \gamma R^{-1})} \quad (12)$$

To evaluate core deformation a range of coaxial samples were printed onto Mylar for ease of removal and processing. The features were carefully cross-sectioned and measured optically to calculate the core and shell cross-sectional areas. Major and minor axes of the core were noted, in addition to the height of the alumina shell above the core. \mathcal{E} was then calculated for each sample and plotted against the ratio of the major (x_i) and minor (y_i) axes of the core. From Figure 5c, one can observe that as \mathcal{E} approaches one, the core eccentricity approaches one, as the magnitude

of the externally deforming gravitational and capillary forces are balanced by the core dynamic yield stress. One could further integrate the capillary forces of the core ink itself into the denominator of Ξ . However, the magnitude of the core capillary force is significantly smaller than the shell core and gravitational forces. Ultimately, through metrics such as Ξ and processing maps generated from flow analysis, both the printing and ink processing parameters may be tailored to fit application needs.

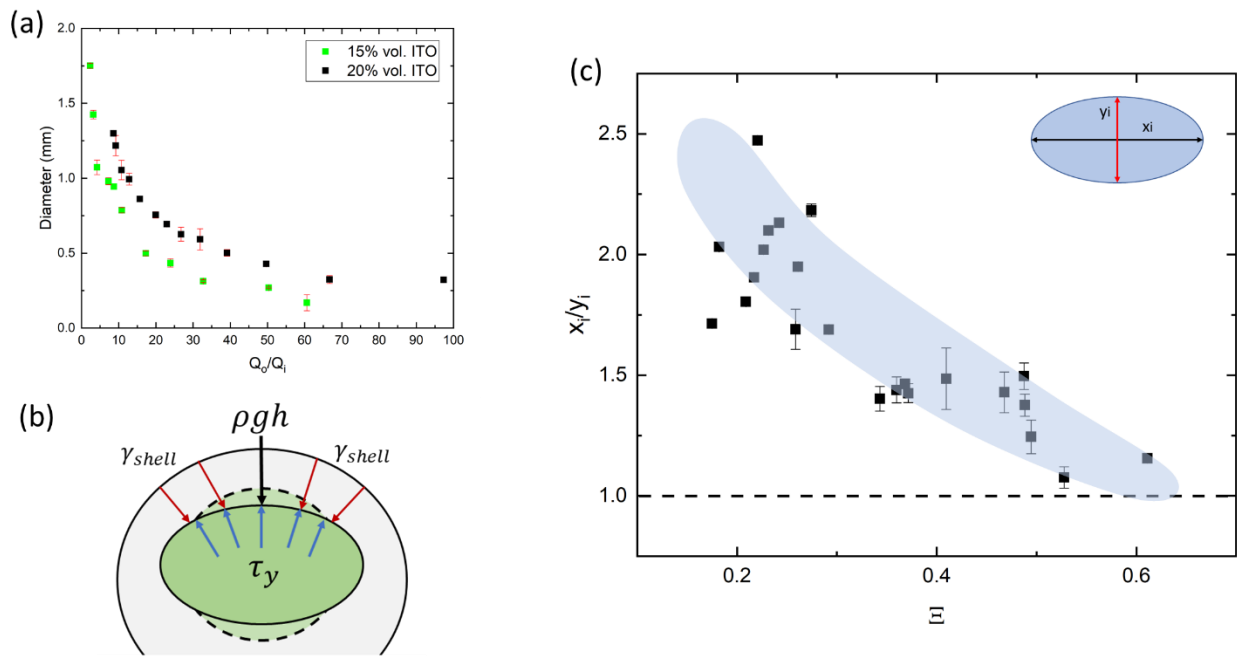


Figure 5. Core fidelity and eccentricity analysis. (a) The effective core diameter vs. flow rate ratio, (b) a simplified force balance acting on the core filament balancing inward and outward radially forces, and (c) the core eccentricity vs. Ξ .

3.4 Sintering, Interfacial Characterization, and Functionality

To demonstrate the potential functionality of the core-shell system in maintaining continuity across a heterogenous substrates, coaxial alumina-ITO lines were printed onto a ceramic surface with visible roughness (Figure 6). Within the substrate are multimodal distributions of

aggregate, which vary by several millimeters and perturb the surface. Within the ink-substrate system, both the alumina shell and refractory material are aqueous based. Therefore, the alumina shell forms an intimate interface with the substrate, mitigating the ‘foreign body’ issue typically associated with embedded sensing elements. However, the minimal binder content and large storage modulus help to limit spreading and promote fidelity retention, highlighted by the hemispherical coaxial cross-section (Figure 6b). The dashed red line in Figure 6b details the ability of the shell to conform to the substrate, while shielding the ITO core (green circle).

To evaluate shrinkage, samples printed on Mylar and the refractory substrate were sintered to 1250°C. Figure A6 shows the alumina core shrinks approximately 4% laterally while shrinking 2% vertically. This minimal shrinkage may be attributed to the bimodal particle distribution and enhanced packing fraction, thus reducing shrinkage, and enabling compatibility with dense substrates. Across core systems, the 15 vol% ITO core shrinks more than the 20 vol% core in both the lateral and vertical directions. This difference is likely attributable to the difference in solids loading. Ultimately, complemented by the limited difference in the shrinkage and the core-shell coefficients of thermal expansion, no catastrophic delamination of the interface is observed (Figure 6c). However, in dissimilar materials, or those with larger differences in thermal expansion, interfacial failure may be a concern and a future area of study. Additionally, through EDX interfacial scans, there is no observable material diffusion or failures observed along the core-shell interface. Figure 6d details a sharp interfacial transition, with the core region distinctly consisting of indium and tin, while the shell consists of aluminum and oxygen. Minimal carbon residue remains within the system following burnout and sintering.

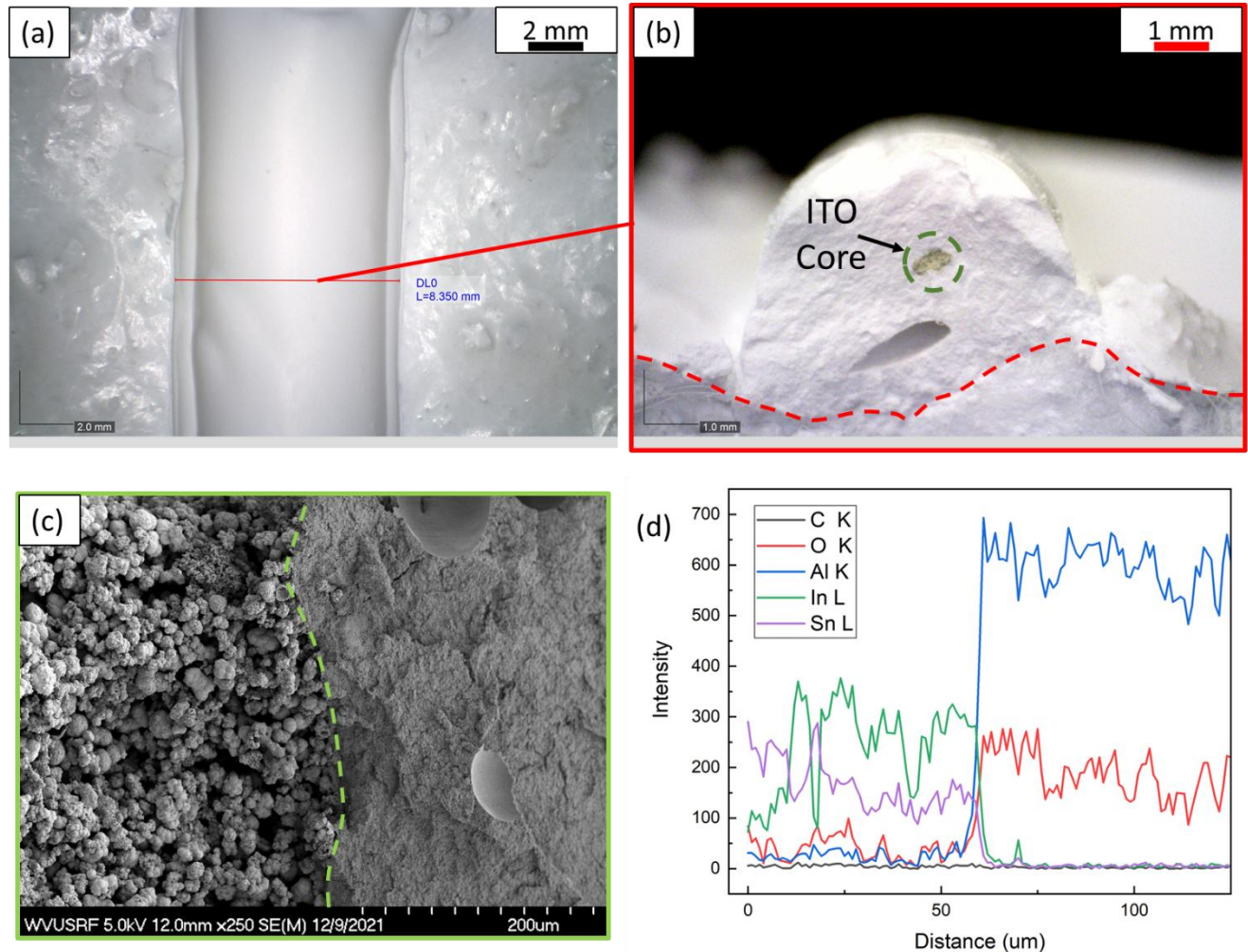


Figure 6. (a) A coaxial thermistor printed directly onto a wet and heterogenous refractory substrate. (b) Optical cross-sectional image demonstrating shell conformability to the substrate surface. (c) Cross-sectional SEM image of the core (left) and shell (right) interface of a sintered sample. (d) Results of an EDS line scan detailing a sharp transition in composition at the interface.

Finally, to demonstrate system functionality, a coaxial Alumina-ITO sample was printed and cycled to 600 °C to assess the system’s ability to detect changes in temperature. For analysis of stability, the furnace temperature was held at 600 °C for two-hours. Figure 7a and 7b show some instability during the ramp up and down but do promisingly reveal stability during the two-hour hold at 600 °C. We attribute the instability during temperature ramps to mobility and instabilities

within the contacts, as the instabilities are only observed during the ramp cycles. Moreover, despite the moderate hysteresis observed in Figure 7a, the system functionality is reflected by the maintained continuity and relative stability during the temperature hold. While there is room for improvement, this data shows promise in utilizing coaxial ceramic DIW to address the manufacturing challenges facing the in-situ deposition of high temperature materials or structural health monitoring systems.

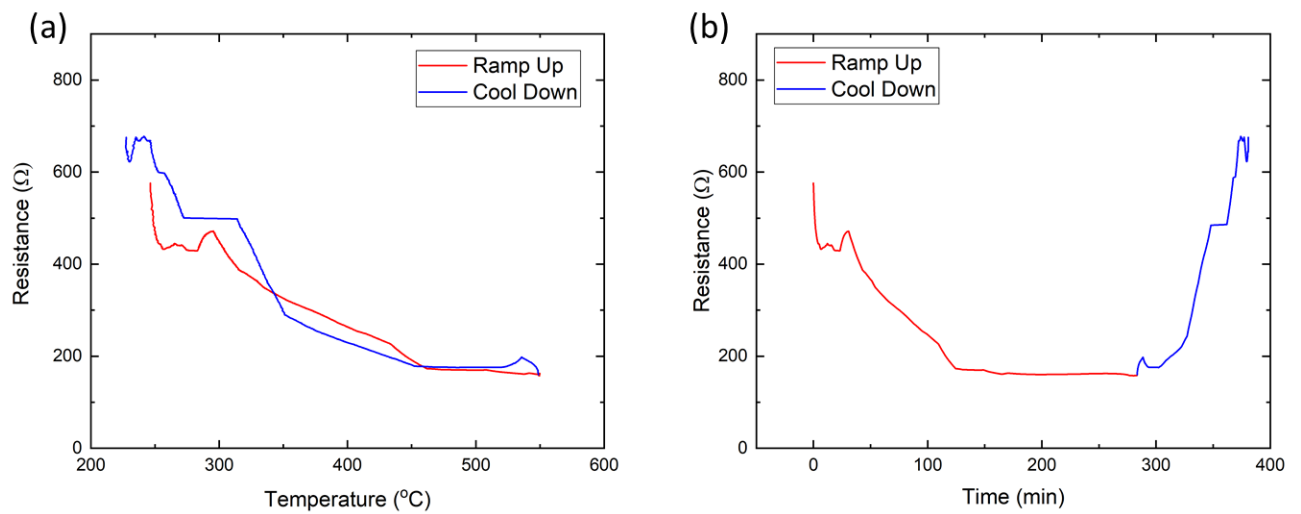


Figure 7. Resistance measurements as a function of time and temperature during a ramp and two-hour hold at 600C. (a) Resistance versus temperature, revealing moderate system hysteresis and instability in the ramp phases. (b) Resistance versus time for the coaxial ceramic system, detailing stability during the two-hour hold. Instability during the ramps is attributed to mobility of the contacts, and not a reflection of ITO instabilities.

3. Conclusion

In summary, we have engineered a ceramic coaxial DIW material suite compatible with heterogenous substrates accomplished through ink engineering and the application of microfluidic inspired process characterization. Importantly, our approach of addressing manufacturing

challenges from a materials perspective, instead of a hardware approach, expands the application space of DIW. Through rheological and ink engineering approaches, rough and heterogenous substrates such as those found in industrial settings become a new DIW frontier. This work specifically demonstrates the potential of ceramic coaxial DIW to overcome common limitations of embedded high temperature electrical conductors, such as poor interfacial adhesion. Using the coaxial material suite, functional components such as conductive ITO may be deposited on previously inaccessible substrates. Moreover, we demonstrate the applicability of microfluidic co-flow principles to assess stable and unstable coaxial DIW regimes, which may be expanded to future non-Newtonian DIW ink compositions. Finally, the adaptation of the dimensionless quantity E restates the importance of physically modeling deformations within DIW. Integrating both computational and physical descriptions of processing aims to elucidate the governing parameters - both material and processing - within the system, as well as the driving forces of deformation. Ultimately, this work provides a physical and experimental approach to modeling coaxial DIW materials, helping to explore the variables which influence stable processing and feature fidelity, while simultaneously expanding the DIW application space. This framework may further be used as a template to guide optimizations of governing print or material parameters such as the extrusion flow rate and the ink apparent viscosity.

ASSOCIATED CONTENT

Supporting Information.

The following files are available free of charge.
COMSOL Flow Simulation Details; Flow Simulation Figures; SEM Images of Coaxial Samples;
Shrinkage and Sintering of the Core Shell Features (PDF)

AUTHOR INFORMATION

Corresponding Author

*To whom the correspondence should be addressed. Tel: +1-304-293-3420, E-mail: kostas.sierros@mail.wvu.edu

Author Contributions

The manuscript was written through contributions of all authors. All authors have given approval to the final version of the manuscript.

Funding Sources

This work has been supported by the U.S. Department of Energy: Project DE-FE0021825.

ACKNOWLEDGMENT

We would like to thank the West Virginia University Shared Research Facilities for the assistance in materials characterization.

ABBREVIATIONS

EDX, Energy Dispersive X-Ray Spectroscopy; SEM, Scanning Electron Microscopy; Al₂O₃, Aluminum Oxide; ITO, Indium Tin Oxide

REFERENCES

- (1) Dutta, C.; Kumar, J.; Das, T. K.; Sagar, S. P. Recent Advancements in the Development of Sensors for the Structural Health Monitoring (SHM) at High-Temperature Environment: A Review. *IEEE Sens. J.* **2021**, *XX* (XX), 1–13. <https://doi.org/10.1109/JSEN.2021.3075535>.
- (2) Petrie, C. M.; Sridharan, N.; Hehr, A.; Norfolk, M.; Sheridan, J. Higherature Strain

- Monitoring of Stainless Steel Using Fiber Optics Embedded in Ultrasonically Consolidated Nickel Layers. *Smart Mater. Struct.* **2019**, *28* (8). <https://doi.org/10.1088/1361-665X/ab2a27>.
- (3) Petrie, C. M.; Schrell, A. M.; Richardson, M. D. *Performance of Embedded Sensors in 3D Printed SiC*; 2021.
- (4) Ghazanfari, A.; Li, W.; Leu, M. C.; Zhuang, Y.; Huang, J. Advanced Ceramic Components with Embedded Sapphire Optical Fiber Sensors for High Temperature Applications. *Mater. Des.* **2016**, *112*, 197–206. <https://doi.org/10.1016/j.matdes.2016.09.074>.
- (5) Chilles, J. S.; Croxford, A.; Bond, I. P. Design of an Embedded Sensor, for Improved Structural Performance. *Smart Mater. Struct.* **2015**, *24* (11). <https://doi.org/10.1088/0964-1726/24/11/115014>.
- (6) Yang, J. C.; Mun, J.; Kwon, S. Y.; Park, S.; Bao, Z.; Park, S. Electronic Skin: Recent Progress and Future Prospects for Skin-Attachable Devices for Health Monitoring, Robotics, and Prosthetics. *Advanced Materials*. Wiley-VCH Verlag November 1, 2019. <https://doi.org/10.1002/adma.201904765>.
- (7) Maazouz, Y.; Montufar, E. B.; Guillem-Marti, J.; Fleps, I.; Ohman, C. ; Persson, C.; Ginebra, M. P. Robocasting of Biomimetic Hydroxyapatite Scaffolds Using Self-Setting Inks †. **2014**. <https://doi.org/10.1039/c4tb00438h>.
- (8) Lin, K.; Sheikh, R.; Romanazzo, S.; Roohani, I. 3D Printing of Bioceramic Scaffolds- Barriers to the Clinical Translation: From Promise to Reality, and Future Perspectives. *Materials*. MDPI AG 2019. <https://doi.org/10.3390/ma12172660>.

- (9) Serra, T.; Mateos-Timoneda, M. A.; Planell, J. A.; Navarro, M. 3D Printed PLA-Based Scaffolds: A Versatile Tool in Regenerative Medicine. *Organogenesis*. 2013. <https://doi.org/10.4161/org.26048>.
- (10) Elsayed, H.; Chmielarz, A.; Potoczek, M.; Fey, T.; Colombo, P. Direct Ink Writing of Three Dimensional Ti₂AlC Porous Structures. *Addit. Manuf.* **2019**, *28*, 365–372. <https://doi.org/10.1016/j.addma.2019.05.018>.
- (11) Li, Y.; Li, L.; Li, B. Direct Ink Writing of Three-Dimensional (K, Na)NbO₃-Based Piezoelectric Ceramics. *Mater. (Basel, Switzerland)* **2015**, *8* (4), 1729–1737. <https://doi.org/10.3390/ma8041729>.
- (12) Rueschhoff, L.; Costakis, W.; Michie, M.; Youngblood, J.; Trice, R. Additive Manufacturing of Dense Ceramic Parts via Direct Ink Writing of Aqueous Alumina Suspensions. *Int. J. Appl. Ceram. Technol.* **2016**, *13* (5), 821–830. <https://doi.org/10.1111/ijac.12557>.
- (13) Duchi, S.; Onofrillo, C.; O’Connell, C. D.; Blanchard, R.; Augustine, C.; Quigley, A. F.; Kapsa, R. M. I.; Pivonka, P.; Wallace, G.; Di Bella, C.; Choong, P. F. M. Handheld Co-Axial Bioprinting: Application to in Situ Surgical Cartilage Repair. *Sci. Rep.* **2017**, *7* (1), 1–12. <https://doi.org/10.1038/s41598-017-05699-x>.
- (14) Milojević, M.; Vihar, B.; Banović, L.; Miško, M.; Gradišnik, L.; Zidarič, T.; Maver, U. Core/Shell Printing Scaffolds for Tissue Engineering of Tubular Structures. *J. Vis. Exp.* **2019**, *2019* (151), 1–10. <https://doi.org/10.3791/59951>.
- (15) Yu, I.; Chen, R. An Experimental and Numerical Study on Coaxial Extrusion of a Non-

- Newtonian Hydrogel Material. *J. Manuf. Sci. Eng. Trans. ASME* **2021**, *143* (8), 1–10.
<https://doi.org/10.1115/1.4050181>.
- (16) Zhang, S.; Lu, L.; Wang, S.; Yuan, F.; Xuan, S.; Gong, X. Coaxial Direct Ink Writing of Shear Stiffening Gel/Ecoflex Composite for Customized Insoles. *Compos. Part B* **2015**, *46*, 1.
- (17) Xu, J.; Zhang, X.; Liu, Y.; Zhang, Y.; Nie, H. Y.; Zhang, G.; Gao, W. Selective Coaxial Ink 3D Printing for Single-Pass Fabrication of Smart Elastomeric Foam with Embedded Stretchable Sensor. *Addit. Manuf.* **2020**, *36* (July), 101487.
<https://doi.org/10.1016/j.addma.2020.101487>.
- (18) Othman, M. H. D.; Droushiotis, N.; Wu, Z.; Kelsall, G.; Li, K. High-Performance, Anode-Supported, Microtubular Sofc Prepared from Single-Step-Fabricated, Dual-Layer Hollow Fibers. *Adv. Mater.* **2011**, *23* (21), 2480–2483. <https://doi.org/10.1002/adma.201100194>.
- (19) Meng, X.; Gong, X.; Yin, Y.; Yang, N. T.; Tan, X.; Ma, Z. F. Microstructure Tailoring of YSZ/Ni-YSZ Dual-Layer Hollow Fibers for Micro-Tubular Solid Oxide Fuel Cell Application. *Int. J. Hydrogen Energy* **2013**, *38* (16), 6780–6788.
<https://doi.org/10.1016/j.ijhydene.2013.03.088>.
- (20) Meng, X.; Yang, N.; Gong, X.; Yin, Y.; Ma, Z. F.; Tan, X.; Shao, Z.; Liu, S. Novel Cathode-Supported Hollow Fibers for Light Weight Micro-Tubular Solid Oxide Fuel Cells with an Active Cathode Functional Layer. *J. Mater. Chem. A* **2015**, *3* (3), 1017–1022.
<https://doi.org/10.1039/c4ta04635h>.
- (21) Wang, Z.; Luan, C.; Zhu, Y.; Liao, G.; Liu, J.; Li, X.; Yao, X.; Fu, J. Integrated and Shape-

- Adaptable Multifunctional Flexible Triboelectric Nanogenerators Using Coaxial Direct Ink Writing 3D Printing. *Nano Energy* **2021**, *90* (PA), 106534. <https://doi.org/10.1016/j.nanoen.2021.106534>.
- (22) Corker, A.; Ng, H. C. H.; Poole, R. J.; García-Tuñón, E. 3D Printing with 2D Colloids: Designing Rheology Protocols to Predict “printability” of Soft-Materials. *Soft Matter* **2019**, *15* (6), 1444–1456. <https://doi.org/10.1039/c8sm01936c>.
- (23) Chan, S. S. L.; Sesso, M. L.; Franks, G. V. Direct Ink Writing of Hierarchical Porous Alumina-Stabilized Emulsions: Rheology and Printability. *J. Am. Ceram. Soc.* **2020**, *103* (10), 5554–5566. <https://doi.org/10.1111/jace.17305>.
- (24) Chan, S. S. L.; Pennings, R. M.; Edwards, L.; Franks, G. V. 3D Printing of Clay for Decorative Architectural Applications: Effect of Solids Volume Fraction on Rheology and Printability. *Addit. Manuf.* **2020**, *35*.
- (25) Xu, C.; Quinn, B.; Lebel, L. L.; Therriault, D.; L', G.; Espérance, E. Multi-Material Direct Ink Writing (DIW) for Complex 3D Metallic Structures with Removable Supports. *ACS Appl. Mater. Interfaces* **2019**, *11*, 36. <https://doi.org/10.1021/acsami.8b19986>.
- (26) Rueschhoff, L.; Costakis, W.; Michie, M.; Youngblood, J.; Trice, R. Additive Manufacturing of Dense Ceramic Parts via Direct Ink Writing of Aqueous Alumina Suspensions. *Int. J. Appl. Ceram. Technol.* **2016**, *13* (5), 821–830. <https://doi.org/10.1111/ijac.12557>.
- (27) Cipollone, D.; Yang, H.; Yang, F.; Bright, J.; Liu, B.; Winch, N.; Wu, N.; Sierros, K. A. 3D Printing of an Anode Scaffold for Lithium Batteries Guided by Mixture Design-Based

- Sequential Learning. *J. Mater. Process. Technol.* **2021**, *295* (January), 117159. <https://doi.org/10.1016/j.jmatprotec.2021.117159>.
- (28) Smay, J. E.; Cesarano, J.; Lewis, J. A. Colloidal Inks for Directed Assembly of 3-D Periodic Structures. *Langmuir* **2002**, *18*, 5429–5437. <https://doi.org/10.1021/la0257135>.
- (29) Sommer, M. R.; Alison, L.; Minas, C.; Tervoort, E.; Rühls, P. A.; Studart, A. R. 3D Printing of Concentrated Emulsions into Multiphase Biocompatible Soft Materials. *Soft Matter* **2017**, *13* (9), 1794–1803. <https://doi.org/10.1039/C6SM02682F>.
- (30) Peng, E.; Wei, X.; Garbe, U.; Yu, D.; Edouard, B.; Liu, A.; Ding, J. Robocasting of Dense Yttria-Stabilized Zirconia Structures. *J. Mater. Sci. Ceram.* **2018**, *53*. <https://doi.org/10.1007/s10853-017-1491-x>.
- (31) Smay, J. E.; Gratson, G. M.; Shepherd, R. F.; Joseph Cesarano III; Lewis, J. A. Directed Colloidal Assembly of 3D Periodic Structures. *Adv. Mater.* **2002**, *14* (18).
- (32) Franks, G. V.; Tallon, C.; Studart, A. R.; Sesso, M. L.; Leo, S. Colloidal Processing: Enabling Complex Shaped Ceramics with Unique Multiscale Structures. *J. Am. Ceram. Soc.* **2017**, *100* (2), 458–490. <https://doi.org/10.1111/jace.14705>.
- (33) Feichtinger, A.; Scholten, E.; Sala, G. Effect of Particle Size Distribution on Rheological Properties of Chocolate. *Food Funct.* **2020**, *11* (11), 9547–9559. <https://doi.org/10.1039/d0fo01655a>.
- (34) Wiśniewska, M.; Urban, T.; Grządka, E.; Zarko, V. I.; Gun'ko, V. M. Comparison of Adsorption Affinity of Polyacrylic Acid for Surfaces of Mixed Silica-Alumina. *Colloid Polym. Sci.* **2014**, *292* (3), 699–705. <https://doi.org/10.1007/s00396-013-3103-x>.

- (35) Michaels, A. S.; Morelos, O. Polyelectrolyte Adsorption by Kaolinite. *Ind. Eng. Chem.* **1955**, *47* (9), 1801–1809. <https://doi.org/10.1021/ie50549a029>.
- (36) Leiva, K.; Sepúlveda, C.; Garcia, R.; Fierro, J. L. G.; Reyes, P.; Ghampson, I. T.; Baeza, P.; Villarroel, M.; Escalona, N. Effect of Mo Content in Mo(x)/g-AL₂O₃ Catalysts over the Conversion of 2-Methoxyphenol as Lignin-Derivates Components. *J. Chil. Chem. Soc.* **2013**, *58* (4), 1947–1951. <https://doi.org/10.4067/S0717-97072013000400007>.
- (37) Farooq, M. The Determination of Point Zero Charge (PZC) of Al₂O₃-MgO Mixed Oxides. In *2011 National Postgraduate Conference*; IEEE, 2011.
- (38) Novak, S.; Kalin, M. The Effect of PH on the Wear of Water-Lubricated Alumina and Zirconia Ceramics. *Tribol. Lett.* **2004**, *17* (4), 727–732. <https://doi.org/10.1007/s11249-004-8080-2>.
- (39) Goharibajestani, Z.; Akhlaghi, O.; Akaoglu, C.; Afghah, F.; Khani, N.; Hodaiei, A.; Koc, B.; Akbulut, O. Incorporating Steric Hindrance into the Additive Design Enables a Robust Formulation of Alumina Ink for Extrusion-Based 3D Printing. *ACS Appl. Polym. Mater.* **2019**, *1* (12), 3279–3285. <https://doi.org/10.1021/acsapm.9b00704>.
- (40) Herschel, W. H.; Bulkley, R. Konsistenzmessungen von Gummi-Benzollösungen. *Kolloid-Zeitschrift* **1926**, *39* (4), 291–300. <https://doi.org/10.1007/BF01432034>.
- (41) M'Barki, A.; Bocquet, L.; Stevenson, A. Linking Rheology and Printability for Dense and Strong Ceramics by Direct Ink Writing. *Sci. Rep.* **2017**, *7* (1), 1–10. <https://doi.org/10.1038/s41598-017-06115-0>.
- (42) J K Nunes; Tsai, S. S. H.; Wan, J.; Stone, H. A. Dripping and Jetting in Microfluidic

- Multiphase Flows Applied to Particle and Fiber Synthesis. *J. Phys. D* **2013**, *10* (12), 5014–5023. <https://doi.org/10.1088/0022-3727/46/11/114002>.Dripping.
- (43) Utada, A. S.; Fernandez-Nieves, A.; Stone, H. A.; Weitz, D. A. Dripping to Jetting Transitions in Coflowing Liquid Streams. *Phys. Rev. Lett.* **2007**, *99* (9), 1–4. <https://doi.org/10.1103/PhysRevLett.99.094502>.
- (44) Zhu, P.; Wang, L. Passive and Active Droplet Generation with Microfluidics: A Review. *Lab Chip* **2017**, *17* (1), 34–75. <https://doi.org/10.1039/C6LC01018K>.
- (45) Li, M.; Tian, X.; Schreyer, D. J.; Chen, X. Effect of Needle Geometry on Flow Rate and Cell Damage in the Dispensing-Based Biofabrication Process. *Biotechnol. Prog.* **2011**, *27* (6), 1777–1784. <https://doi.org/10.1002/btpr.679>.
- (46) van Hout, R.; Murugan, S.; Mitra, A.; Cukurel, B. Coaxial Circular Jets-a Review. *Fluids* **2021**, *6* (4), 1–22. <https://doi.org/10.3390/fluids6040147>.
- (47) Heugten, W. G. N. van. Shape and Stability in Liquid Threads and Jets : A Link to Droplet Formation, 2015.

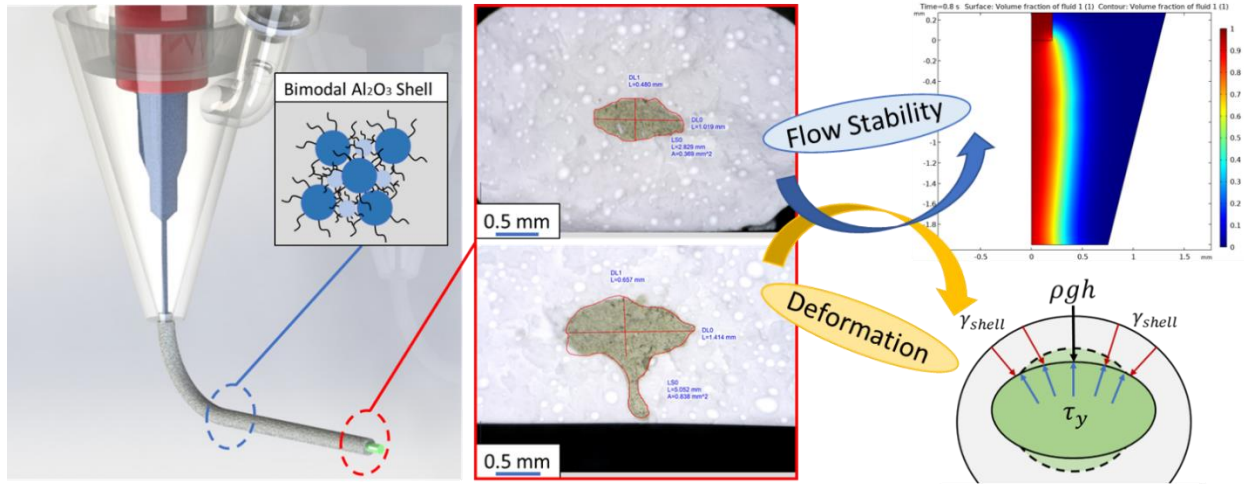


Figure 8: GRAPHICAL ABSTRACT